Research Article Vol. 31, No. 9 / 24 Apr 2023 / Optics Express 13851
Optics EXPRESS

Evaluation of eight band SuperDove imagery for aquatic applications

QUINTEN VANHELLEMONT*

Royal Belgian Institute of Natural Sciences, Operational Directorate Natural Environments, Vautierstraat 29, 1000 Brussels, Belgium
quinten.vanhellemont@naturalsciences.be

Abstract: Planet's SuperDove constellation is evaluated for remote sensing of water targets. SuperDoves are small satellites with on board eight band PlanetScope imagers that add four new bands compared to the previous generations of Doves. The Yellow (612 nm) and Red Edge (707 nm) bands are of particular interest to aquatic applications, for example in aiding the retrieval of pigment absorption. The dark spectrum fitting (DSF) algorithm is implemented in ACOLITE for processing of SuperDove data, and its outputs are compared to matchup data collected using an autonomous pan-and-tilt hyperspectral radiometer (PANTHYR) installed in the turbid waters of the Belgian Coastal Zone (BCZ). Results for 35 matchups from 32 unique SuperDove satellites indicate on average low differences with PANTHYR observations for the first seven bands (443–707 nm), with mean absolute relative differences (MARD) 15–20%. The mean average differences (MAD) are between -0.01 and 0 for the 492–666 nm bands, i.e. DSF results show a negative bias, while the Coastal Blue (444 nm) and Red Edge (707 nm) show a small positive bias (MAD 0.004 and 0.002). The NIR band (866 nm) shows a larger positive bias (MAD 0.01), and larger relative differences (MARD 60%). Root mean squared differences (RMSD) are rather flat at around 0.01 with peaks in the bands with highest water reflectance of around 0.015. The surface reflectance products as provided by Planet (PSR) show a similar average performance to DSF, with slightly larger and mostly positive biases, except in both Green bands, where the MAD is close to 0. MARD in the two Green bands is a bit lower for PSR (9.5–10.6%) compared to DSF (9.9–13.0%). Higher scatter is found for the PSR (RMSD 0.015–0.020), with some matchups showing large, spectrally mostly flat differences, likely due to the external aerosol optical depth (τ_a) inputs not being representative for these particular images. Chlorophyll *a* absorption (a_{Chl}) is retrieved from PANTHYR measurements, and the PANTHYR data are used to calibrate a_{Chl} retrieval algorithms for SuperDove in the BCZ. Various Red band indices (RBI) and two neural networks are evaluated for a_{Chl} estimation. The best performing RBI algorithm, i.e. the Red band difference (RBD), showed a MARD of 34% for DSF and 25% for PSR with positive biases of 0.11 and 0.03 m^{-1} respectively for 24 PANTHYR a_{Chl} matchups. The difference in RBD performance between DSF and PSR can be largely explained by their respective average biases in the Red and Red Edge bands, which are opposite signs for DSF (negative bias in the red), and positive for both bands for PSR. Mapping of turbid water a_{Chl} and hence chlorophyll *a* concentration (C) using SuperDove is demonstrated for coastal bloom imagery, showing how SuperDove data can supplement monitoring programmes.

1. Introduction

Applications of decametre scale optical satellite imagery have increased significantly in the past decade, thanks to freely available imagery from Landsat 8/9 (launched in 2013 and 2021), and Sentinel-2 A/B (launched in 2015 and 2017). In the aquatic realm, the imagery from these satellite missions has been used for mapping of water turbidity [1–3], chlorophyll *a* concentration [4,5], bathymetry [6,7], and floating vegetation [8]. These sensor systems are designed for land applications, and aquatic applications usually push the systems to their limits in terms

#483418 https://doi.org/10.1364/OE.483418
Journal © 2023 Received 16 Dec 2022; revised 7 Mar 2023; accepted 8 Mar 2023; published 12 Apr 2023

Optics EXPRESS

of top-of-atmosphere calibration, radiometric performance, and accuracy of the atmospheric correction [9]. The launch of several commercial satellites with metre scale optical imagers (e.g. Pléiades, WorldView, PlanetScope) has lead to similar applications at even smaller spatial scales [10–12].

Planet first launched prototype four band (Blue, Green, Red, NIR) Dove satellites in 2013 and has launched several flocks of Doves since. For over five years they have continuously operated a constellation of Dove satellites with the aim of imaging the Earth's land surface every day at 3 m resolution. This imagery inevitably also covers inland and coastal waters, and Dove imagery has been evaluated for mapping of various water quality parameters [12–15] and bathymetry [16,17]. With the launch of the third generation "SuperDove" satellites starting in April 2019, Planet can provide improved image quality and spectral resolution, with a more robust top-of-atmosphere vicarious calibration using near simultaneous Sentinel-2 data [18], i.e. relying on the Sentinel-2 calibration. The number of bands on the SuperDoves is increased from four to eight, adding a shorter wavelength "Coastal" Blue band, as well as Green, Yellow, and Red Edge bands. This much more complete spectral coverage could enable additional parameter retrievals at high spatial and temporal resolution, if the top-of-atmosphere calibration is accurate, and if the hundreds of individual satellites in the constellation can provide interoperable data. Especially the Yellow (612 nm) and Red and Red Edge (666 and 707 nm) bands may prove to be useful for retrieving pigment concentration in turbid and productive waters, e.g. using the phycocyanin absorption maximum near 620 nm [19,20] or the chlorophyll *a* absorption peak near 670 nm [21,22].

In the present paper the eight band SuperDove data are evaluated for water applications, with a focus on turbid coastal waters. The Dark Spectrum Fitting (DSF) algorithm [10,23] is adapted to SuperDove and integrated into the open source ACOLITE processor. The official Planet Surface Reflectance (PSR) product and DSF outputs are compared to in situ measurements collected by an autonomous hyperspectral radiometer deployed in Belgian turbid coastal waters. Chlorophyll *a* absorption (a_{Chl}) is retrieved using simple Red band index (RBI) algorithms using the SuperDove Red, Red Edge, and NIR bands, as well as 7 and 8 band Neural Networks, and their outputs are compared to in situ derived values. To inform users of SuperDove data products, drawbacks of PSR compared to DSF for targets not at normal pressure are illustrated for a high altitude lake. Glint correction methods for clear, i.e. low turbidity waters, and the potential for bathymetry retrieval are both demonstrated for PSR and DSF.

2. Data and methods

2.1. Study areas

This paper focuses on the turbid near-shore waters of the Belgian Coastal Zone (BCZ) in the southern North Sea, more specifically those around the Blue Accelerator platform (callsign RT1, at 51.2464°N, 2.9193°E). RT1 is located just outside the port of Oostende, about 1 km from shore, and about 0.5 km from the port entrance (Fig. 1). The BCZ is a shallow (< 50 m) shelf sea, with a well mixed water column as a result of strong tides and high winds. Water turbidity varies at diurnal and seasonal scales by the resuspension of sediments, and phytoplankton blooms occur in spring and summer [24]. At short temporal and spatial scales, horizontal advection of water masses occurs as a result of tidal currents. The average water depth at RT1 is 9 m, with average tidal range of 5 m and average wave height of 0.9 m. Due to high turbidity there is no bottom visibility. Average wind speed at the Oostende Weather Station (OWS, about 1.3 km from RT1) was 5.0 ms^{-1} during the deployment duration, with 5th and 95th percentiles of 1.7 and 9.6 ms^{-1}.

2.2. PANTHYR data

PANTHYR [25] is an autonomous pan-and-tilt hyperspectral radiometer, consisting of two TriOS RAMSES radiometers, one for measuring down- and upwelling radiances (L_d and L_u)

Optics EXPRESS

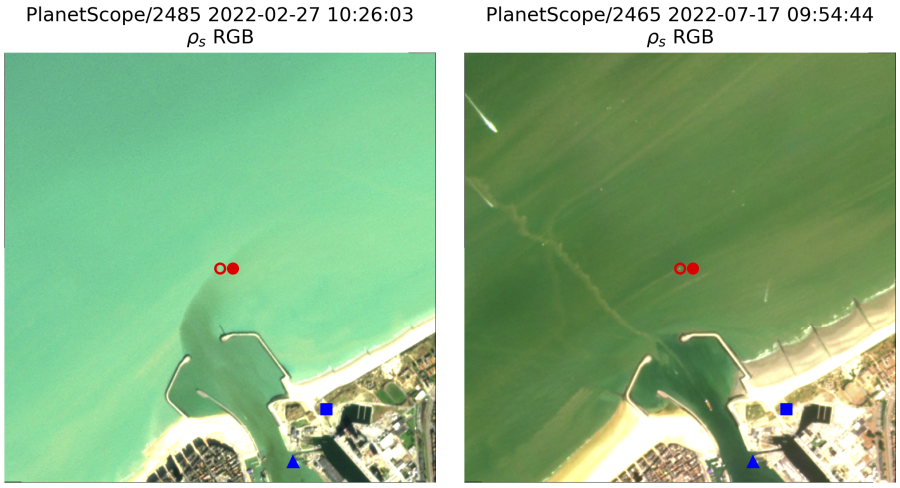

Fig. 1. SuperDove RGB ρ_s composites from 3x3 km subsets centred on RT1. Images were taken during flood tide on 2022-02-27 (left), and during ebb tide on 2022-07-17 (right). The open and closed circles show the platform and matchup locations, the square and triangle the Oostende Weather Station and Tide Gauge. Note the darker waters from the port outflow reaching RT1 in the left image, and the turbid wake in the right image created by the tidal current around the platform monopile [1].

and one for measuring downwelling irradiance (E_d). The measurement protocol and processing largely follows [26,27], with the exception that measurements are made sequentially rather than simultaneously. A single measurement cycle consists of three E_d, three L_d, eleven L_u, three L_d, and three E_d replicates. Replicates are quality controlled and mean averaged. Measurements are interpolated from the sensor wavelengths to a regular 2.5 nm wavelength step from 355 to 945 nm. A full description of the measurement cycle and processing available in [25]. Measurements are performed every 20 minutes for a number of relative azimuth angles to the sun (90°, 135°, 225°, 270°) depending on sun and instrument position, avoiding measurements with platform obstructions and structure shadows. The upwelling radiance is measured at a 40° nadir angle to minimise glint on the water surface. Wind speed is retrieved from 6-hourly NCEP/MET modeled data to retrieve the fraction of L_d reflected at the air-water interface (ρ_F) from the lookup tables of [26]. The water-leaving radiance (L_w) and reflectance (ρ_w) can then be retrieved:

$$L_w = L_u - \rho_F \cdot L_d, \tag{1}$$

and,

$$\rho_w = \frac{\pi \cdot L_w}{E_d}. \tag{2}$$

PANTHYR measurements made at RT1 between February and October 2022 passing the preliminary quality control [25,27] from the 270° relative azimuth angles were used, as this measurement geometry gives most frequent valid measurements during SuperDove overpasses (between 9:46 and 10:40 UTC in the current dataset). The reflectance envelope of these measurements is presented in Fig. 2. Data from a previous PANTHYR deployment at RT1 (2019–2020) were used for validation of the Ocean and Land Colour Instrument (OLCI) on board of Sentinel-3 A/B [28] and the Operational Land Imager (OLI) on board of Landsat 8, the MultiSpectral Instrument (MSI) on board of Sentinel-2 (S2) A/B, and the previous generation of Planet Doves [14], as well as for the determination of phytoplankton pigments [24].

Optics EXPRESS

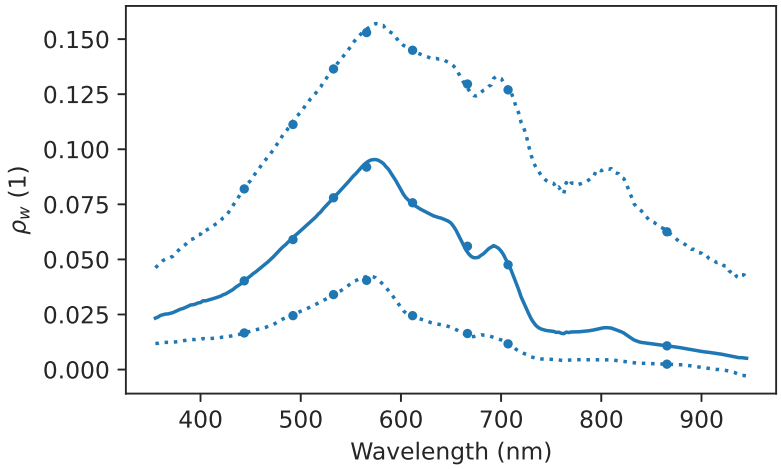

Fig. 2. Median (solid) and 1–99 percentiles (dotted lines) of RT1 PANTHYR ρ_w measured between 2022-02-24 and 2022-10-09 at 270° relative azimuth. Dots represent the data convolved to SuperDove bands, plotted at the band average wavelength.

2.3. Satellite data

2.3.1. SuperDove imagery

SuperDoves are CubeSats in the 3U form factor (10x10x30 cm) with eight band imagers on board, consisting of seven visible (VIS) and one near-infrared (NIR) band (Table 1). The sensor design relative spectral response (RSR) shown in Fig. 3 is used for processing all units in the constellation. Swath width (around 24 km) and pixel size (around 3–4 metres) of the sensors depend on satellite altitude, which varies during their lifetime as a result of orbit decay, as the satellites lack orbit control. SuperDoves do not have an on board calibration system, and hence rely on vicarious methods for the on orbit calibration. The absolute calibration is performed using near-simultaneous SuperDove and S2/MSI observations, and validated with RadCalNet data, with lunar imaging used for monitoring the relative calibration during the sensor's lifetime [18]. Imagery is acquired at a sampling of 1x (3 m) for the Blue to Red bands, and at 0.5x (6 m) for the Red Edge and NIR bands, and at 0.25x (12 m) for the Coastal Blue band. Planet provides the eight band imagery as orthorectified GeoTIFF files with 3x3 metre pixel size through the Planet Explorer website (https://www.planet.com/explorer, accessed 23 November 2022) or the application programming interface (API). Cloud free images covering the RT1 location were obtained through the API both as top-of-atmosphere radiance (TOAR, bundle name analytic_8b_udm2) and surface level reflectance (SR, bundle name analytic_8b_sr_udm2). Images were subset in the API using GeoJSON polygons, to an approximately 3x3 km region centred on RT1, or using a custom polygon for the study areas in the Appendices. Imagery was accessed between 27 September 2022 and 24 November 2022 and was processed at Planet with CMO processor version 4.1.4. Imagery from the same satellite overpass that was split into multiple datasets by Planet was merged in ACOLITE to a single dataset during processing.

2.3.2. ACOLITE/DSF

TOAR products are provided by Planet as unsigned 16 bit integer GeoTIFF files, with metadata that contain multiplicative factors to convert the data to top-of-atmosphere reflectance (ρ_t) or radiance (L_t). Zero values are reserved for the no data mask. ρ_t images were processed using the automated Dark Spectrum Fitting (DSF) algorithm [10,23] as implemented in ACOLITE version 20221114.0 (Python code cloned from https://github.com/acolite/acolite). The DSF uses the

Optics EXPRESS

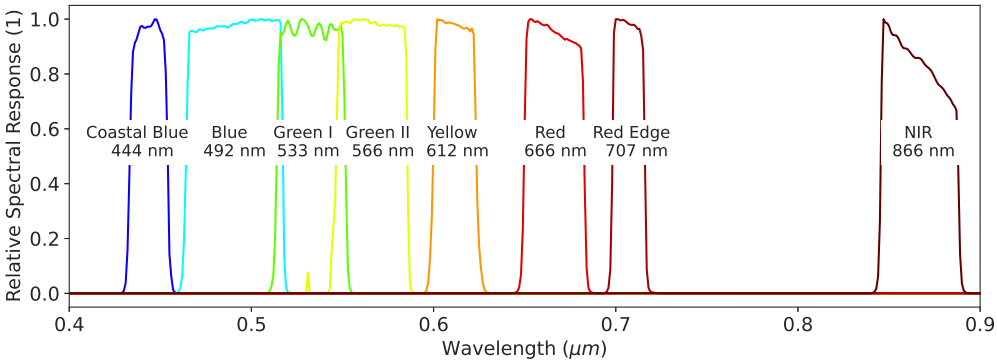

Fig. 3. SuperDove eight band relative spectral response function as provided by Planet.

Table 1. SuperDove band names, centre wavelengths and full width at half maximum in nm as derived from the RSR in Fig. 3.

Band Name	Wavelength (nm)	FWHM (nm)
Coastal Blue	444	20
Blue	492	52
Green I	533	37
Green II	566	38
Yellow	612	23
Red	666	32
Red Edge	707	16
NIR	866	41

observed ρ_t over dark targets in the scene or subscene to construct a dark spectrum (ρ_{dark}), and estimates the aerosol optical depth (τ_a at 550 nm) for each band in this dark spectrum, assuming zero surface level reflectance (ρ_s). The lowest τ_a across all bands is then used for processing, and a choice is made between the available aerosol models. Based on the τ_a and the selected aerosol model, the required parameters for atmospheric correction, i.e. the atmospheric path reflectance (ρ_{path}), two-way total transmittance (T_d and T_u), and the spherical albedo of the atmosphere (S) are retrieved from a lookup table (LUT). The LUTs are generated using the continental (MOD1) and maritime (MOD2) aerosol models in 6SV [29] for four pressure levels (500, 750, 1013, 1000 hPa, representing an elevation range of about 5500 to -700 m) and a wide range of viewing and illumination geometries and aerosol optical depths [14,28]. Surface level reflectance (ρ_s) can then be retrieved from the ρ_t, assuming a uniform Lambertian target [30]:

$$\frac{\rho_t}{T_g} = \rho_{path} + \frac{\rho_s \cdot T_d T_u}{1 - \rho_s \cdot S}, \tag{3}$$

where T_g is the band average gas transmittance, computed using variable concentrations of ozone and water vapour. The DSF was configured to estimate a single τ_a and aerosol model for each 3x3 km image, using the darkest observed ρ_t in each band as ρ_{dark}. The aerosol model giving the lowest root mean squared difference (RMSD) between the ρ_{dark} and ρ_{path} in the two best fitting bands (i.e. those with the lowest estimate of τ_a) was then selected for processing.

Optics EXPRESS

2.3.3. Planet SR

Planet provides standard SR products (PSR) that have been corrected using 6SV with atmospheric parameters obtained from the MODIS/Terra Aerosol Optical Thickness Daily L3 Global 0.05Deg CMA dataset (MOD09CMA, DOI: 10.5067/MODIS/MOD09CMA.NRT.006), [31] resampled to cover the image area from the plate carrée projected data (0.05°, pixel sizes about 5.6 km at the equator, coarser at higher latitudes). PSR data are provided as unsigned 16 bit integer GeoTIFF files with a 1/10000 discretisation factor and no offset. Zero values are reserved for the no data mask and hence the minimum reflectance that can be represented by PSR is 1/10000. Both DSF and PSR share the radiative transfer code used for atmospheric correction, and differ mainly in the manner in which the aerosol model and τ_a are estimated. DSF estimates these parameters from the imagery itself, while PSR relies on external inputs for τ_a and uses the continental aerosol model (MOD1) by default. For atmospheric gas information, DSF uses water vapour and ozone from 6 hourly NCEP Reanalysis2 and daily Aura OMI global datasets, interpolated in space and time to the image centre. PSR retrieves this information also from MOD09CMA, which presumably uses similar ancillary global datasets.

2.4. Matchups

Matchups were extracted from a reference location at 51.2464°N, 2.9206°E, about 90 metres east of RT1, in order to avoid direct and indirect platform contamination [14]. An 11x11 box (33x33 m) was extracted centred on the reference location and the mean average and standard deviation were computed for this box. The mean values were used in the matchup comparison, while the standard deviations were used as error bars on the plots. The closest PANTHYR observation in time within 30 minutes was used, linearly interpolated to the satellite overpass time if bounding observations within 30 minutes were available, and convolved to the SuperDove RSR (Fig. 3). For PANTHYR data, half the absolute difference between the bounding observations is used as error bars on the plots. SuperDove pixels were masked using simple thresholds, i.e. if any ρ_t > 0.3 or when ρ_t NIR > 0.1. A reduced major axis (RMA) regression, i.e. the line bisecting two ordinary least squares (OLS) regressions swapping datasets on abscissa and ordinate, was performed per band. The following average statistics were computed between in situ (x) and satellite (y) data: the mean average difference (MAD), representing the bias,

$$MAD = \sum_{i=1}^{n} \frac{y_i - x_i}{n}, \tag{4}$$

the root mean square difference (RMSD), representing the scatter,

$$RMSD = \sqrt{\sum_{i=1}^{n} \frac{(y_i - x_i)^2}{n}}, \tag{5}$$

and the mean absolute relative difference (MARD),

$$MARD = \sum_{i=1}^{n} \frac{|y_i - x_i|}{0.5 \cdot (y_i + x_i) \cdot n}. \tag{6}$$

2.5. Turbid water chlorophyll a retrieval

The retrieval of chlorophyll a absorption (a_{Chl}, in m^{-1}) from SuperDove bands is evaluated using the hyperspectral PANTHYR measurements. The a_{Chl} feature at around 670 nm is visible in many of the hyperspectral data recorded by PANTHYR at RT1 (Fig. 2). This feature is not always clearly present after convolution to SuperDove bands, or in the SuperDove observations (see later

Optics EXPRESS

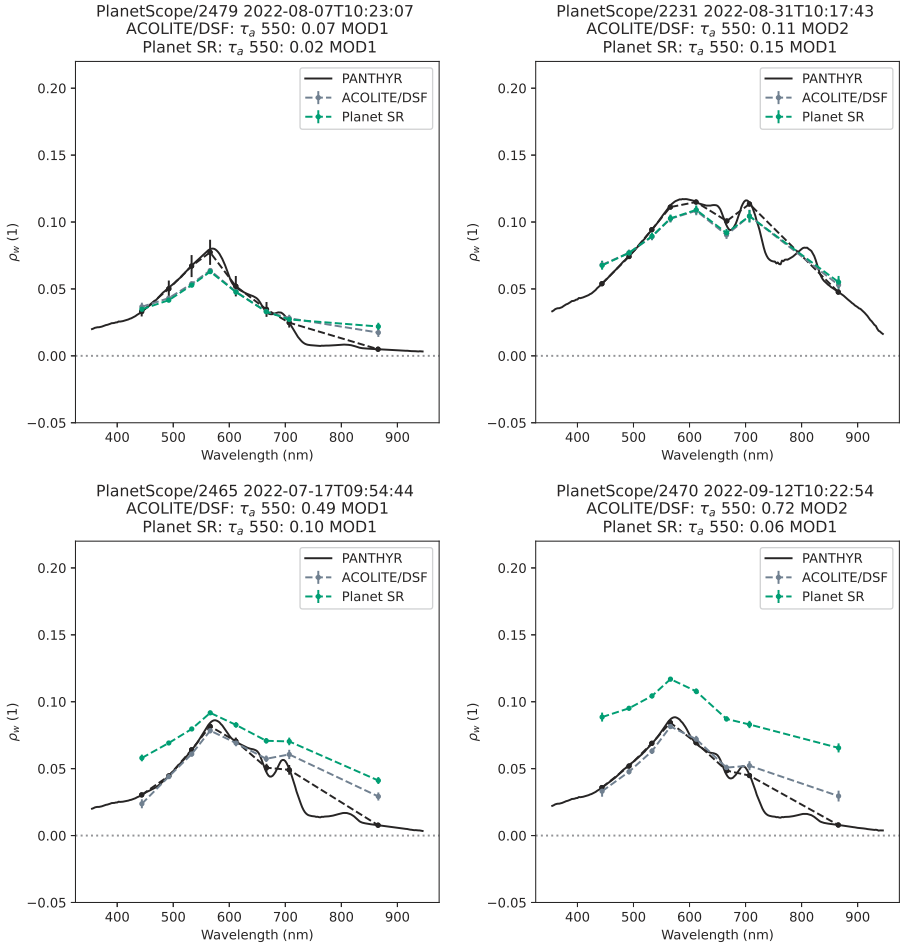

Fig. 4. Spectral plots for selected matchups between SuperDove and PANTHYR, with good correspondence (top) and significant differences (bottom) between DSF and PSR. The solid black line is the hyperspectral PANTHYR data, dots are resampled to the SuperDove RSR. Error bars indicate half the range between bounding PANTHYR data taken 20 minutes apart and the standard deviation in a 11x11 pixel box for the satellite data. The plot title shows the τ_a at 550 nm and the aerosol model per processor.

in Fig. 4), even though it has Red and Red Edge bands centred on 666 and 707 nm. Whether the 707 nm band provides a good enough reference to estimate a_{Chl} in the Red band, depends on the position of the Red Edge peak within the Red Edge band, which depends on chlorophyll *a* concentration (C) and water turbidity [32]. Here the PANTHYR data is used to retrieve a_{Chl} at 672 nm with the chlorophyll *a* retrieval using an adaptive two-band algorithm (CRAT) [22]. CRAT finds the wavelength in the region 700–740 nm where ρ_w is equal to ρ_w 672 nm, and with the assumption of equal backscatter coefficients, a_{Chl} at 672 nm can be retrieved by the difference in pure water absorption (a_w) at the two wavelengths. a_w is here taken from WOPP [33] at 20 °C and 36 PSU. CRAT is rather robust, since it does not need an estimate of backscatter coefficients, but can only be applied to spectra where the local maximum ρ_w between 700–740 nm is greater than or equal to ρ_w 672 nm. PANTHYR data are convolved to the SuperDove bands, and various Red band indices (RBI) are fitted to the a_{Chl} using an ordinary least squares (OLS) regression.

Optics EXPRESS

a_{Chl} can then be estimated from the SuperDove RBI:

$$a_{Chl} = (RBI - b) \cdot m^{-1}, \tag{7}$$

where b and m are the offset and slope from the RBI specific OLS regression. C can be easily retrieved from a_{Chl} by division by the mass-specific chlorophyll a absorption (a^*_{Chl}) at 672 nm, taken here to be 0.016 $m^2 mg^{-1}$. Various RBI using ρ_w in the Red (R), Red Edge (RE) and NIR bands were evaluated: the Red band difference [34] (RBD):

$$RBD = RE - R, \tag{8}$$

the two and three Red band ratio algorithms [35,36] (RBR2, RBR3):

$$RBR2 = R^{-1} \cdot RE, \tag{9}$$

$$RBR3 = (R^{-1} - RE^{-1}) \cdot NIR, \tag{10}$$

and the normalised difference chlorophyll index [37] (NDCI):

$$NDCI = (RE - R) \cdot (RE + R)^{-1}. \tag{11}$$

Neural networks (NN) were also evaluated for the retrieval of a_{Chl} directly from the SuperDove spectrum. The convolved PANTHYR dataset was used to train models with seven (NN7B) and eight (NN8B) inputs, and five hidden, fully connected layers of eight neurons with rectified linear unit activation function. The NIR band was excluded from the NN7B in order to test sensitivity to the presence of NIR information, which can be quite noisy in the SuperDove imagery. Input data were normalised using the mean and standard deviation in each band, and training was performed over 1000 epochs with in each epoch 10% of data randomly excluded for validation.

3. Results and discussion

3.1. Matchups

35 matchups between SuperDove and PANTHYR at RT1 were obtained. These 35 matchups originate from 32 unique SuperDove satellites, with 3 satellites each providing 2 matchups. Example spectra are shown in Fig. 4 for two matchups with good correspondence between DSF and PSR and two with a significant difference. The in situ hyperspectral data show turbid waters with rather high ρ_w of 0.07–0.12 at 560 nm (Remote sensing reflectance, $Rrs = \rho_w \cdot \pi^{-1}$, of about 0.02–0.04 sr^{-1}), and a characteristic turbid water bump at 810 nm caused by a local minimum in the pure water absorption. The Red a_{Chl} feature at around 670 nm is clear in the hyperspectral data, thanks to the high water signal, and the reference provided by the Red Edge region (700–740 nm). PANTHYR data resampled to the SuperDove bands do not always clearly show this a_{Chl} feature, as a result of the changing position of the Red Edge peak in the relatively broad SuperDove bands. For example, the peak is located largely left of the SuperDove band on 2022-07-17 and 2022-09-12 (lower row of Fig. 4), while it is almost centered on the band on 2022-08-31 (top right panel of Fig. 4). The position of the peak with respect to the SuperDove bands will largely determine the possibility, and accuracy, of the turbid water a_{Chl} retrieval using RBI. The difference of the Red Edge spectral shape between convolved PANTHYR and the SuperDove observation on 2022-07-17 (bottom left plot of Fig. 4) can be explained by strong spatial variability around the site, and different water properties at the PANTHYR and matchup reference location (see also the right RGB composite in Fig. 1).

Matchup statistics are summarised spectrally in Fig. 5, and scatter plots for individual bands are shown in Fig. 6 for the first four bands (444–566 nm) and in Fig. 7 for the last four bands (612–866 nm). Overall, an impressive consistency is found for the 32 different satellites, with

Optics EXPRESS

low relative errors in the bands with the highest turbid water signal (566 and 612 nm). The largest relative differences are found for the Coastal Blue (444 nm) and NIR (866 nm) bands, characterised respectively by the largest atmospheric and lowest water leaving signals. Similar performance is found for PSR and DSF, although PSR retrieves slightly higher absolute, and largely positive, biases compared to DSF, except in both Green bands (533 and 556 nm). For both processors, the bias follows largely the inverted shape of a water spectrum, with the PSR bias shifted up compared to DSF. The DSF results shows a spectral feature in the RMSD, with a local peak in the Green I, II and Yellow bands (533–612 nm), where also the largest (negative) biases are retrieved. The matchup average scatter is lower for DSF than for PSR in all bands, which is mostly a result of differences in τ_a and aerosol model used in both methods.

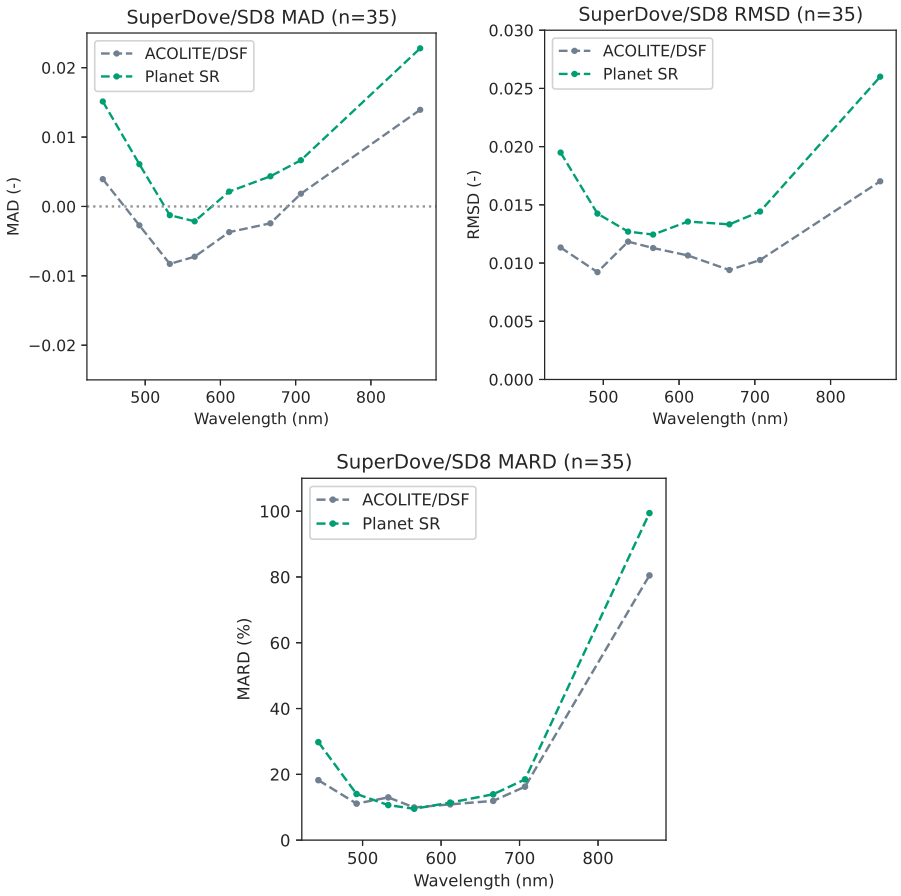

Fig. 5. Spectral errors for the DSF (grey) and PSR (Green) SuperDove PANTHYR matchups. Top left: mean average difference (MAD), and right: root mean squared difference (RMSD), bottom: mean absolute relative difference (MARD)

In the PSR dataset, all 35 matchups used the continental aerosol model (MOD1), with an average τ_a (550 nm) of 0.11 (±0.08). For DSF, 25 matchups used MOD1, and 10 used MOD2 (maritime aerosol), with an average τ_a (at 550 nm) of 0.24 (±0.17). DSF retrieved higher τ_a for 25 out of the 35 matchups, respectively 18/25 and 7/10 in the cases where MOD1 and MOD2 were used. For the 25 matchups where DSF selected MOD1, PSR and DSF retrieved an average τ_a of respectively 0.12 (±0.09) and 0.23 (±0.13). DSF most frequently used the NIR (17), Coastal Blue (8), and Red Edge (7) for τ_a estimation, mainly from water targets (27/35). Although a

Optics EXPRESS

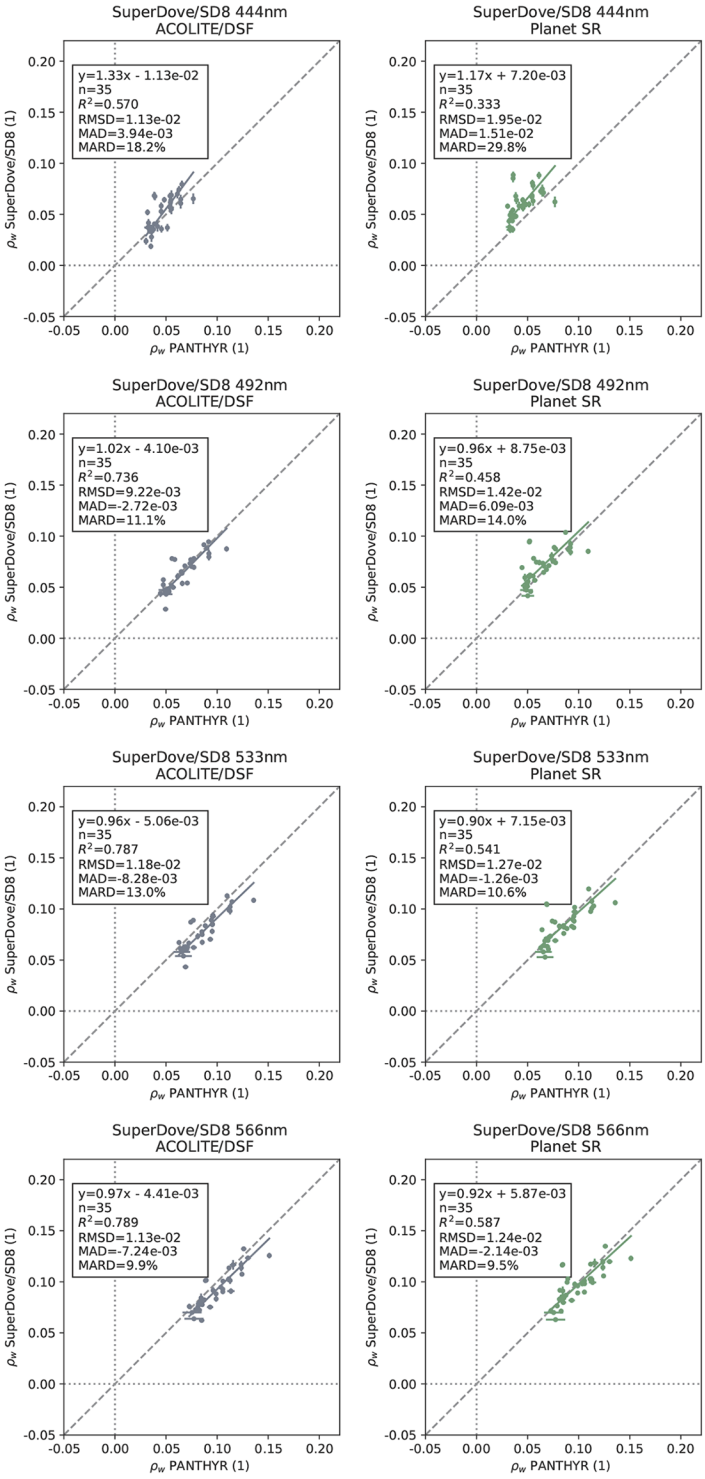

Fig. 6. Scatter plots for matchups between SuperDove and PANTHYR for bands 1–4 (444–566 nm), left: DSF, right: PSR. Error bars show half the range between bounding PANTHYR (horizontal) and the standard deviation in a 11x11 pixel box (vertical).

Optics EXPRESS

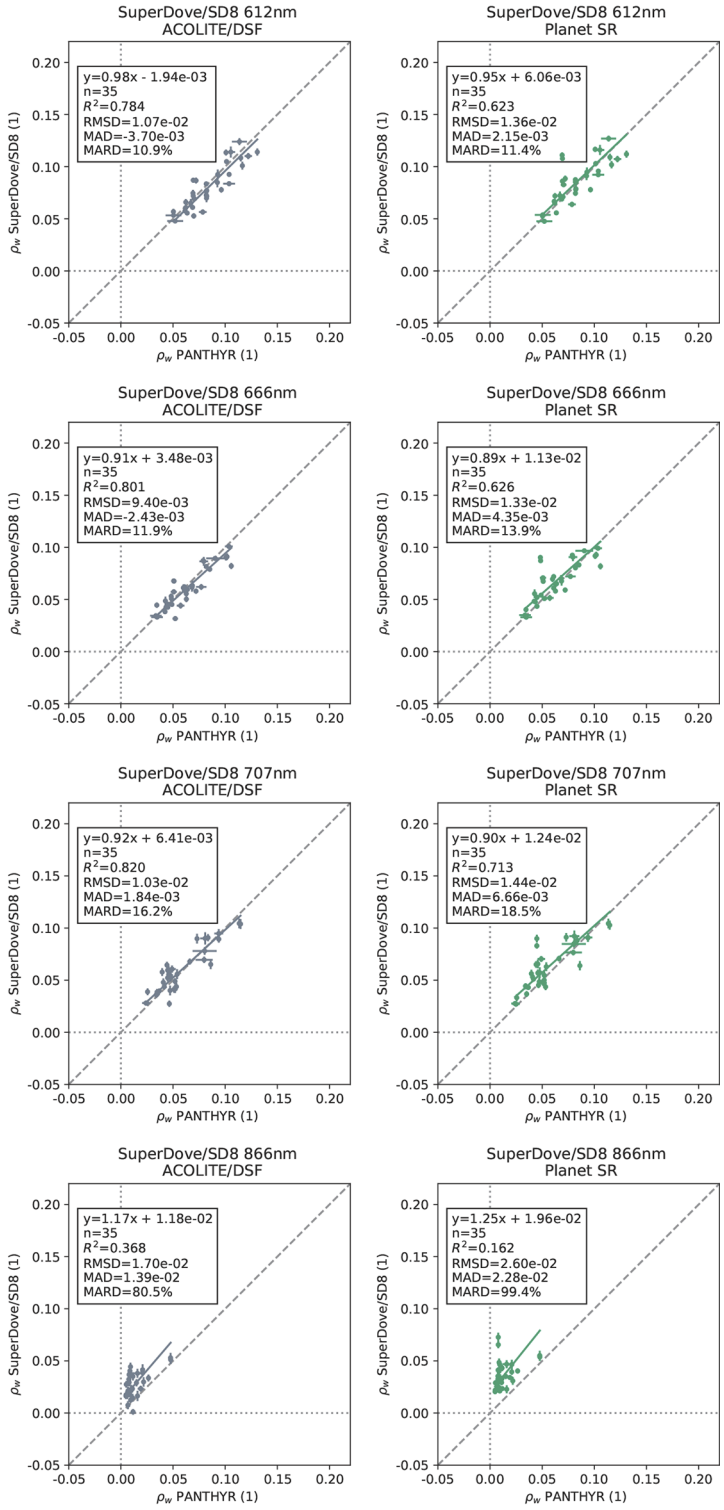

Fig. 7. Same as Fig. 6 but for bands 5–8 (612–866 nm).

Optics EXPRESS

comparison of τ_a retrievals is not sufficient for ρ_s validation, it is clear here that the differences in τ_a can explain the shift in the bias spectrum between PSR and DSF. The results indicate that the PSR ancillary τ_a may be biased low for water applications, potentially a result of assumptions made in MOD09CMA, or the pixel sizes of MODIS or the plate carrée projection.

PSR assumes normal atmospheric pressure, while DSF can take pressure variations into account, either by using a user supplied pressure or elevation, or by using elevation from a digital elevation model (DEM), e.g. as provided by Copernicus or the Shuttle Radar Topography Mission (SRTM). For targets at an elevation significantly different from sea level, the current PSR products are not sufficient, and variable atmospheric pressure needs to be taken into account in the atmospheric correction (see Appendix A). RT1 is at sea level and hence apart from the differences in the used aerosol model and τ_a as described above, PSR/DSF results are comparable. At the Oostende Weather Station (OWS) atmospheric pressure measurements mean averaged 1017 hPa during the PANTHYR deployment, with 5–95 percentiles between 1003–1033 hPa. For a typical sun-sensor geometry and τ_a, taken here as the mean averages of the matchup dataset, i.e. solar zenith angle, $\theta_s = 44°$, view zenith angle, $\theta_v = 3.5°$, relative azimuth angle, $\Delta\phi = 131°$, and $\tau_a = 0.24$ (using MOD1), these pressure ranges lead to ρ_{path} differences of -1.0% and +1.7% in the Coastal Blue band (444 nm), i.e. the band with highest ρ_{path}. Only 1.4% of observations at OWS deviate >20 hPa from normal pressure and, hence, by assuming normal pressure ρ_{path} at 444 nm is generally within ±1.7%. Lower differences are found for other bands, with a minimum of ±0.9% in the NIR. Although atmospheric pressure can vary due to weather conditions (±20 hPA in the BCZ), elevation derived pressure is a good estimate for the purpose of atmospheric correction. A general application of the DEM derived pressure in ACOLITE/DSF can be recommended. For elevated targets the current version of PSR should be avoided.

Satellite imagery of water targets is contaminated by varying levels of adjacency effects and sun glint on the air-water interface. Adjacency effects from nearby areas with a high spectral contrast to water can cause significant issues for aquatic applications, and land vegetation adjacency may introduce spurious NIR and Red Edge features in the water spectra. For SuperDove, the NIR band will be most impacted by uncorrected glint and adjacency, which may represent a large factor of the retrieval uncertainty in this band. These errors are compounded by the high noise level in the NIR, calibration difficulties over low signal targets, as well as the potential presence of floating materials and whitecaps. Glint and adjacency effects are currently not corrected for in either PSR or DSF, and the development of correction methods for metre-scale satellite imagery are active areas of research, especially for turbid and productive waters. Currently, one method for correcting adjacency effects for aquatic applications, the similarity environment correction [38] (SIMEC), is available in iCor for operational processing of decametre scale imagery from Landsat and Sentinel-2 [39]. SIMEC relies on an assumption of fixed water reflectance ratios from the NIR similarity spectrum [27] which should be avoided for turbid and productive waters, especially for the SuperDove band set that only covers the red to NIR wavelengths with three broad bands. For high resolution imagery, adjacency correction methods add a significant computational burden due to the amount of pixels that need to be integrated at the scale of typical atmospheric point spread functions. For satellite imagery at RT1, adjacency effects represent a rather small error, as most of the background signal comes from similar waters, and the generally strong water signal. Sun glint correction methods either rely on constraining water reflectance [40] or by using observations in bands with negligible water leaving signal [41,42]. NIR based sun glint correction methods can give rather robust results for SuperDove over clear waters (Appendix B), but these methods use assumptions that are invalid over turbid and productive waters. In the BCZ, sun glint on the air water interface is limited to summer conditions for nadir viewing imagers, and the most severe sun glint is currently removed by masking thresholds.

Optics EXPRESS

3.2. Turbid water chlorophyll a retrieval

CRAT was used to retrieve a_{Chl} at 672 nm from the RT1 PANTHYR data, with valid retrievals for 1345 measurements from the end of March to early October 2022 (Fig. 8). The time-series of a_{Chl} shows strong spring (end of April) and summer (mid July and end of August) blooms. The highlighted points have ρ_w NIR > 0.02 and correspond to ebb tide measurements under certain conditions. The average spectra of these highlighted points show characteristics of higher particulate backscattering, but with lower CDOM absorption. PANTHYR derived SuperDove RBI are plotted as function of the CRAT a_{Chl} in Fig. 9. Points with high ρ_w NIR are also highlighted in Fig. 9, but they are not treated separately in the OLS fits. Strong linear correlations are found for all RBI, with best results for RBD and RBR3. For a_{Chl} <0.5 m^{-1}, a larger scatter is found for the RBI indicating that the SuperDove Red and Red Edge band characteristics are less suitable in these conditions, and especially so for a_{Chl} < 0.4 m^{-1}. At lower a_{Chl} the Red Edge peak shifts to shorter wavelengths and will be partially or fully outside the SuperDove Red Edge band, resulting in it being undetectable. The RBI involving a ratio, i.e. RBR2, RBR3, and NDCI, seem more sensitive to the type of water encountered at RT1, with the more turbid waters found during some ebb tides clearly forming separate relationships for those RBI (orange dots in Fig. 9). The best performing RBI algorithm is here found to be the RBD. RBR3 also performs rather well using the PANTHYR data, but is likely to be negatively impacted by the NIR band performance of the SuperDoves. With the OLS regression coefficients given per RBI in Table 2, a_{Chl} can be retrieved from SuperDove observations using Eq. (7). Both NN7B and NN8B have many more parameters compared to the RBI algorithms, and they were able to outperform them significantly on the calibration dataset, especially thanks to better matching at the lower end of the a_{Chl} range by using the full spectral information. Presumably the NN are able to pick up on more subtle spectral cues that are not captured by the RBI in order to retrieve low a_{Chl}. Data from [43] measured in the BCZ aligns well with the RBI: a_{Chl} relationships found here. For their inland water data more variability, as well as a larger range of a_{Chl}, up to 1.5–2 m^{-1}, was found. For these inland water data, the RBR3 fit proved to be rather robust, while a significant difference was found for RBD, likely as a result of differences in non-algal particulate backscattering in the Belgian coastal and inland waters. The algorithms presented here are not intended to be generally applicable, and should only be considered for waters similar to those encountered in the BCZ.

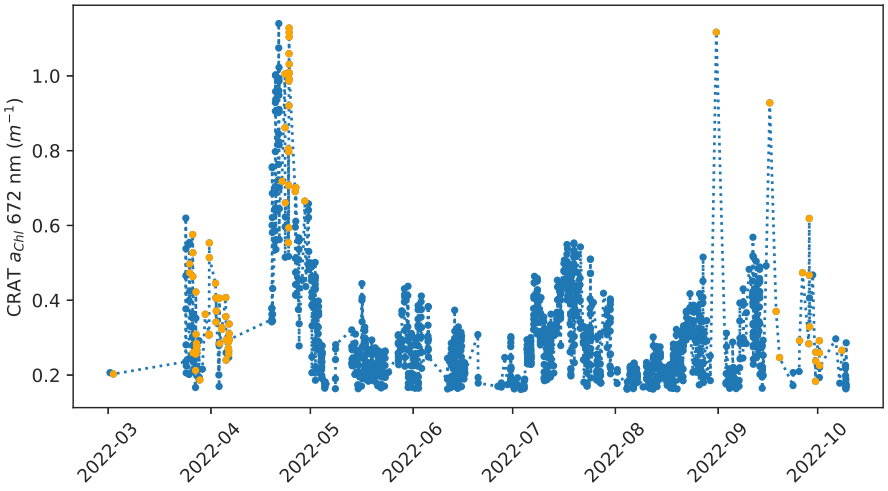

Fig. 8. PANTHYR CRAT a_{Chl} timeseries. Orange dots have ρ_w NIR > 0.02.

Optics EXPRESS

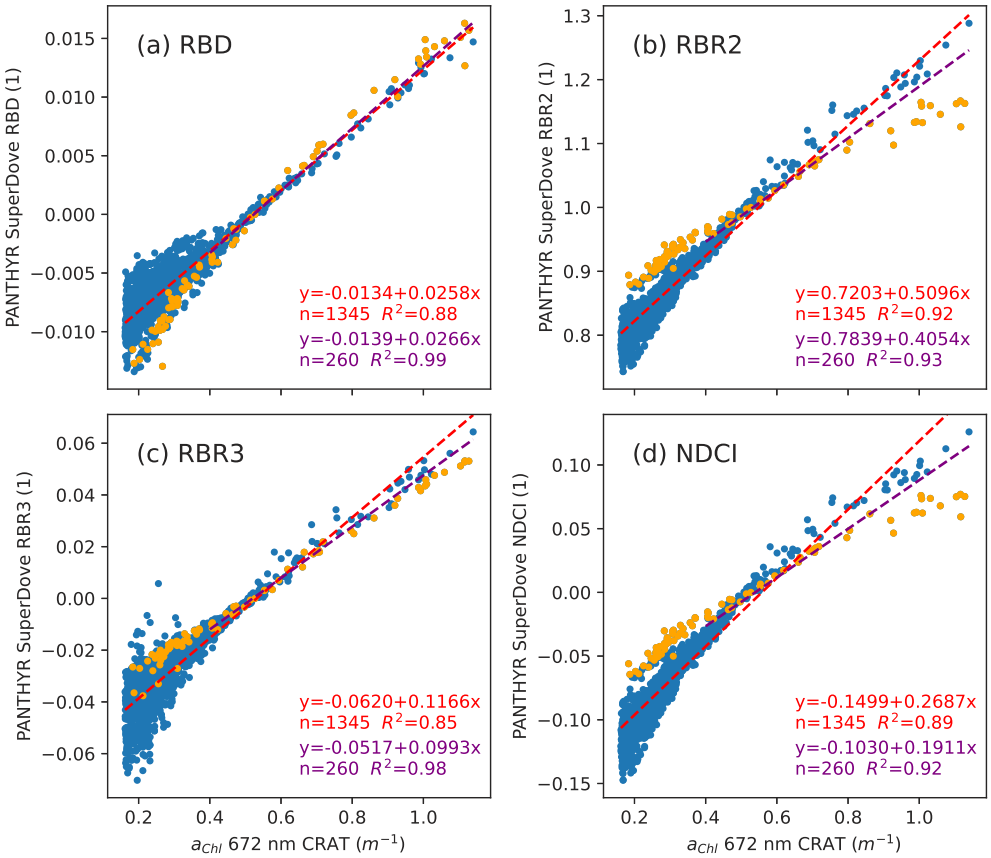

Fig. 9. PANTHYR derived RBI as function of CRAT a_{Chl}, with ordinary least squares (OLS) regression lines. OLS are performed for the whole data range (red) and for a_{Chl} >= 0.4 (purple). Orange dots have ρ_w NIR > 0.02, highlighted for illustration.

Table 2. Calibration and validation results for the BCZ SuperDove a_{Chl} retrieval algorithms.

Algorithm	b (m^{-1})	m (1)	RMSD (m^{-1})	MAD (m^{-1})	MARD (1)
			DSF | PSR	DSF | PSR	DSF | PSR
RBD	-0.0134	0.0258	0.17 | 0.11	0.11 | 0.03	0.34 | 0.25
RBR2	0.7203	0.5096	0.18 | 0.14	0.11 | 0.05	0.34 | 0.25
RBR3	-0.0620	0.1166	0.25 | 0.22	0.11 | -0.08	0.56 | 0.76
NDCI	-0.1499	0.2687	0.19 | 0.15	0.11 | 0.06	0.34 | 0.27
NN7B	–	–	0.24 | 0.19	0.16 | 0.11	0.36 | 0.29
NN8B	–	–	0.20 | 0.12	0.13 | 0.01	0.30 | 0.18

Optics EXPRESS

The performance of the SuperDove a_{Chl} retrieval is evaluated using 24 out of the 35 matchups where CRAT could be applied to the PANTHYR measurement. Fig. 10 shows the results for the RBD and RBR3, the most promising RBI using in situ measurements, and NN8B, for both DSF and PSR. The model calibration and performance statistics are summarised in Table 2 For the RBD, both DSF and PSR give slopes close to 1, but overestimate the a_{Chl} with biases respectively of 0.11 and 0.03 m^{-1}, and DSF gave larger scatter (17 m^{-1}) compared to PSR (11 m^{-1}). On average the PSR products gave better relative performance (MARD) of 24% compared to 33% for DSF. The difference between DSF and PSR is caused by the average reflectance biases found in the Red and Red Edge bands (Fig. 7), which directly impact the RBD retrieval. PSR has biases with the same sign, whereas DSF has biases with opposite sign, with a negative bias for the Red band, leading to an increased RBD and hence increasing its a_{Chl} retrieval. For the RBR3 larger differences are found (MARD 56% for DSF and 76% for PSR) as a result of the inclusion of the SuperDove NIR observation, which has higher noise and retrieval uncertainty. Slopes are 1.50 (DSF) and 1.58 (PSR) mainly as a result of the large positive biases in the NIR band that is used as multiplicative factor in RBR3. For RBR2 and NDCI the MARD were similar to RBD, i.e. 34–35% for DSF, 26–27% for PSR, but with RMA slopes significantly different from 1, i.e. 0.75–0.79 for DSF, 0.64–0.67 for PSR, indicating an underestimation of high a_{Chl}. The NN results gave similar performance overall to the more simple RBI models, with perhaps slightly higher RMSD and MAD. NN8B gave lower errors compared to the NN7B, indicating the NIR band contains information that improves the a_{Chl} retrieval. Both NN seemed to show a tighter grouping at low a_{Chl} in the scatter plots for both DSF and PSR. NN8B applied to PSR data gave the lowest biases and MARD across all algorithms. The better performance compared to DSF is likely due to the average mostly same sign, positive biases in the PSR reflectances.

Retrieval of C from SuperDove imagery is demonstrated in Fig. 11 using a set of images taken during the spring and summer blooms observed in the PANTHYR time-series (Fig. 8). For both of these images, bounding PANTHYR CRAT retrievals are available within 20 minutes. For 2022-04-24, the SuperDove average C retrieved using RBD over a 11x11 pixel box on the reference location was 50 (DSF) and 43 (PSR) $mg \cdot m^{-3}$, whereas PANTHYR bounding observations are 32–44 $mg \cdot m^{-3}$. For 2022-08-29, the SuperDove retrievals are 57 (DSF) and 54 (PSR) $mg \cdot m^{-3}$ with PANTHYR giving 35–42 $mg \cdot m^{-3}$. Due to high variability at short time and length scales there are differences inherent to the PANTHYR and reference locations. Horizontal advection with the tidal current can cause large differences in the PANTHYR field of view even at the 20 minute measurement interval. This effect can be seen as the large error bars for several points in Fig. 6 and 7, and also on the resampled PANTHYR data for the 2022-08-07 matchup (bottom left of Fig. 4). Small scale advection can be directly observed on several pairs of same day SuperDove imagery, with surface features moving 50–150 m on images taken a 3–5 minutes apart on e.g. 2022-08-07, 2022-08-10, and 2022-09-12 (not shown).

Regular, usually monthly, shipborne campaigns are performed in the BCZ using the RV Simon Stevin (operated by VLIZ) and RV Belgica (operated by RBINS) to fulfill various nearshore and offshore monitoring obligations, e.g. for European Union Marine Strategy and Water Framework Directives (MSFD, WFD). No regularly visited stations are present in this 3x3 km subset centred on RT1, and due to vessel draught, regular shipborne measurements cannot be made in the nearshore area. The presence and behaviour of these bloom conditions remain largely unstudied and unreported. The RT1 PANTHYR deployment [24], and the SuperDove C products presented here can hence provide additional information on coastal blooms like these. These nearshore blooms were previously also observed on Sentinel-2 and RapidEye imagery by exploiting their Red Edge bands at 20 and 6.5 m spatial resolution [13]. It was demonstrated with the results in the current paper that the monitoring of these blooms can now be extended by adding the more frequent imagery at 3 m spatial resolution from the SuperDove constellation.

Optics EXPRESS

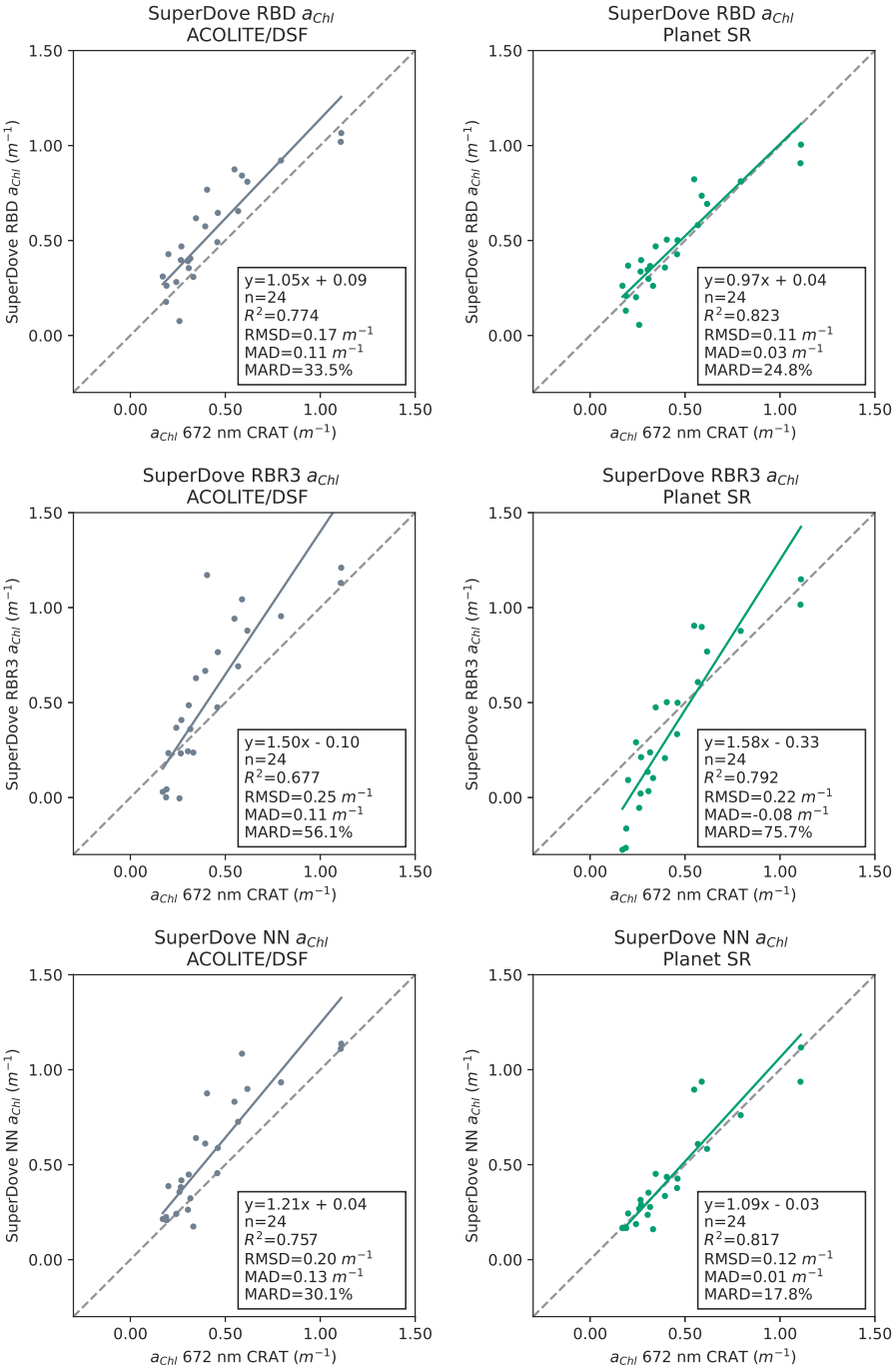

Fig. 10. SuperDove a_{Chl} compared to CRAT for DSF (left) and PSR (right) for RBD (top), RBR3 (middle) and NN8B (bottom). The lines are the RMA regression.

Optics EXPRESS

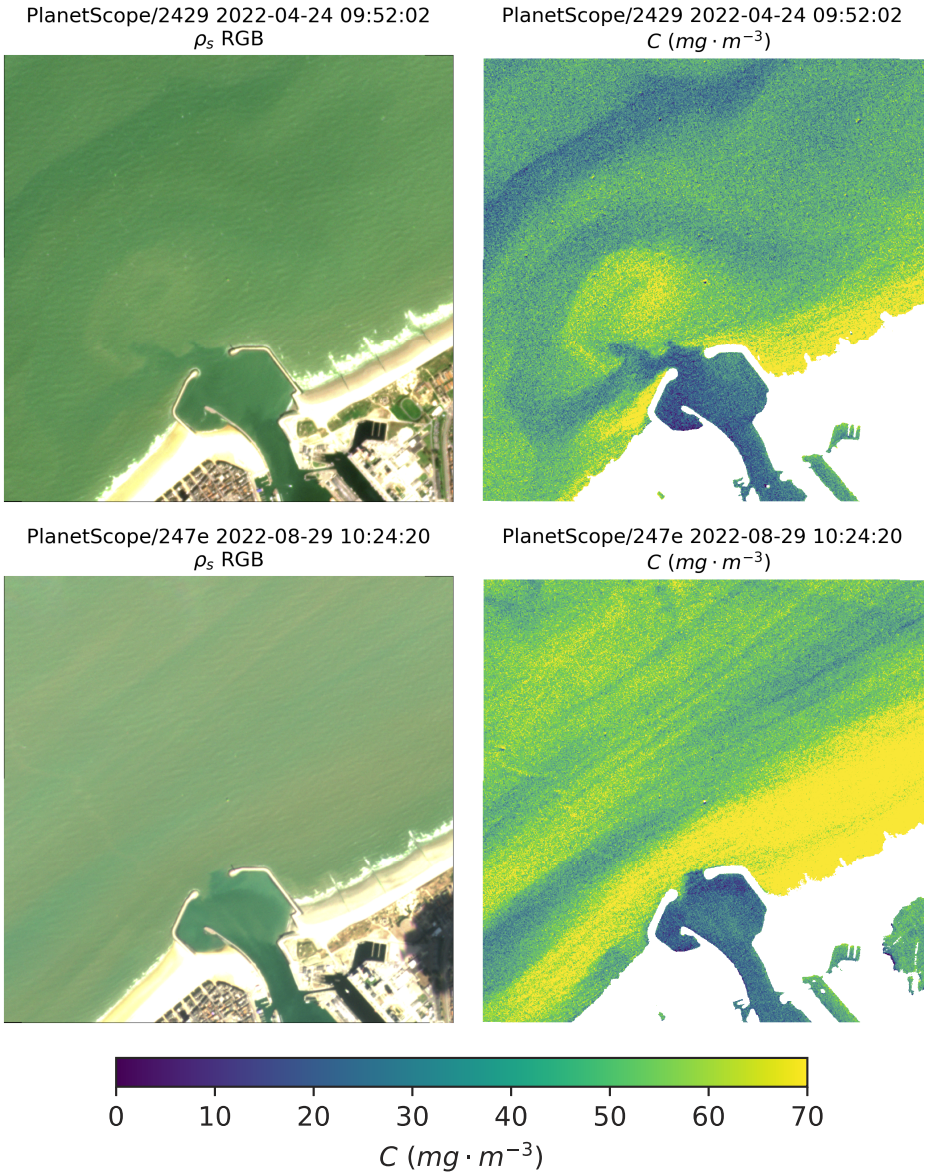

Fig. 11. SuperDove ρ_s RGB composites (left) and DSF/RBD derived C (right) during the spring (top, 2022-04-24) and summer (bottom, 2022-08-29) blooms as observed by PANTHYR (Fig. 8). Non-water pixels are masked using a NIR threshold (ρ_s 866 nm >0.07). An undetected cloud shadow is present on the bottom right plot.

Optics EXPRESS

4. Conclusions

With eight VNIR bands and frequent imagery provided at 3 m resolution, SuperDoves show promise for integration in Coastal and inland water monitoring programmes. Across 35 matchups from 32 unique satellites, SuperDove observations corresponded well to measurements made with a PANTHYR autonomous hyperspectral radiometer in the turbid waters of the BCZ. Good consistency between the various satellites in the constellation was found, with promising performance for turbid water remote sensing. On average DSF and PSR products provided similar results, with low relative errors, i.e. MARD <20% in the VIS, reaching <10% in the bands with highest signal, and rather low biases (MAD between -0.01 and 0.01). Compared to DSF, PSR showed lower average MARD and MAD in two bands, i.e. Green I and II at 533 and 566 nm, albeit with slightly higher scatter (RMSD 0.012). For the other bands, DSF provided lower MAD and MARD, also with lower RMSD. For several matchups PSR overestimated compared to PANTHYR, as a result of using a too low τ_a and thus a too low ρ_{path}, whereas DSF retrieved higher τ_a and hence its outputs more closely matched the in situ data. These results indicate that a better performance may be achieved with image derived compared to ancillary τ_a.

The CRAT algorithm was used to retrieve a_{Chl} from the PANTHYR dataset, and four RBI and two NN algorithms were fitted for the retrieval of a_{Chl} and hence C from the SuperDove bandset. From the RBI algorithms, RBD and RBR3 performed best, with RBR2 and NDCI being rather sensitive to variability in optical properties of the water, indicated by two groups of points separable by ρ_w NIR. The RBD algorithm calibration showed that good performance can be expected for a_{Chl} between 0.5–1.2 m^{-1}, corresponding to mostly positive RBD, and C retrievals between 30–75 $mg \cdot m^{-3}$ (at a^*_{Chl} of 0.016 $m^2 mg^{-1}$). The large range of RBI at low ρ_w and low a_{Chl}, sets a lower bound to the applicability of these algorithms, as a result of the shifting Red Edge peak with respect to the SuperDove bands. In sufficiently turbid waters, the lower bound could be further lowered as indicated by the points with NIR $\rho_w > 0.02$, albeit with slight underestimation in low a_{Chl} conditions. The upper bound is determined by the in situ observation range, and could be extended with measurements at higher a_{Chl}. Not surprisingly, the NN performed much better than the RBI on the calibration dataset, and could also retrieve low a_{Chl} values. Matchups between SuperDove and PANTHYR showed that a_{Chl} could be tracked during the spring and summer blooms in the BCZ. For the RBD, PSR gave better performance than DSF, as a result of its same sign biases in the Red and Red Edge bands. The opposite sign biases for DSF lead to a positive bias in its RBD and hence a_{Chl}. Application of the RBR3 to imagery showed negative impacts by the higher uncertainty and positive bias in the NIR band. For the matchups, the NN performance was similar to, but not significantly better than, the simple RBI algorithms. The near-shore Coastal blooms are currently missed by regular shipborne monitoring campaigns, and SuperDove provides unique capabilities for observing these.

Important considerations for users of SuperDove and ACOLITE/DSF are included in the two Appendices to this paper. Up to a few hundred metres from sea level, the assumption of normal pressure gives rather low errors on the atmospheric correction, and performance of PSR and DSF was found to be comparable. For elevated targets however, atmospheric pressure needs to be taken into account, which is currently not done in PSR. In Appendix A it was shown that DSF can provide more realistic reflectances for high altitude lakes by using DEM derived pressure. Glint correction for clear waters, i.e. where NIR ρ_w can be considered zero, was demonstrated in Appendix B. For these types of targets, at sea level, both PSR and DSF show adequate capabilities of glint removal using the NIR ρ_s observation for light to moderately glinted images. Two automatic methods are integrated into ACOLITE. Thanks to the high observation density of SuperDove, imagery severely affected by glint can usually be discarded, although reasonable performance may be achieved for bright targets (e.g. bright coral sand bottoms). Additional developments are needed for turbid water glint correction, and the correction of adjacency effects, that should ideally be automated and integrated into the atmospheric correction procedure.

Optics EXPRESS

Appendix A: Atmospheric pressure

In this appendix the use of variable atmospheric pressure in the atmospheric correction is demonstrated using two inland water targets. Dongbu Cuo (or Tungpu Co) is a high altitude turbid saline lake in the Tibetan Plateau (at around 31.2951°N, 87.2248°E) with a mean elevation of 4647 m, which corresponds to an atmospheric pressure of about 584 hPa using standard atmospheric parameters. The Sea of Galilee (at around 32.8139°N, 35.5938°E) is the world's lowest freshwater lake, with a mean elevation of -214 m, or an atmospheric pressure of 1039 hPa. Its main water source is the Jordan River, which discharges in to the lake at its northern end. TOAR products for both targets are processed with ACOLITE using two settings: DSF using the Copernicus 30 m DEM [44] and DSF-NP using normal pressure. PSR products are used as is. The top row of Fig. 12 shows two points from Dongbu Cui, P1 from the less turbid southern lake, and P2 from the more turbid northern lake. PSR and DSF-NP retrieve low ρ_s due to overestimation of ρ_{path}, with differences caused by the aerosol type and concentration. The PSR file format does not permit negatives, and the format minimum values (1/10000) are retrieved for the Coastal Blue and Blue bands. DSF gives more realistic turbid water spectra compared to PSR/DSF-NP. The lower row of Fig. 12 shows two points from the Sea of Galilee, P1 close to the Jordan River mouth and P2 more offshore. For this region, a much lower difference with normal pressure, and hence a close agreement between DSF, DSF-NP, and PSR is found. Note the higher ρ_t for the higher pressure, lower altitude targets. For both lakes a rather high NIR signal is retrieved, likely due to uncorrected glint and/or adjacency effects.

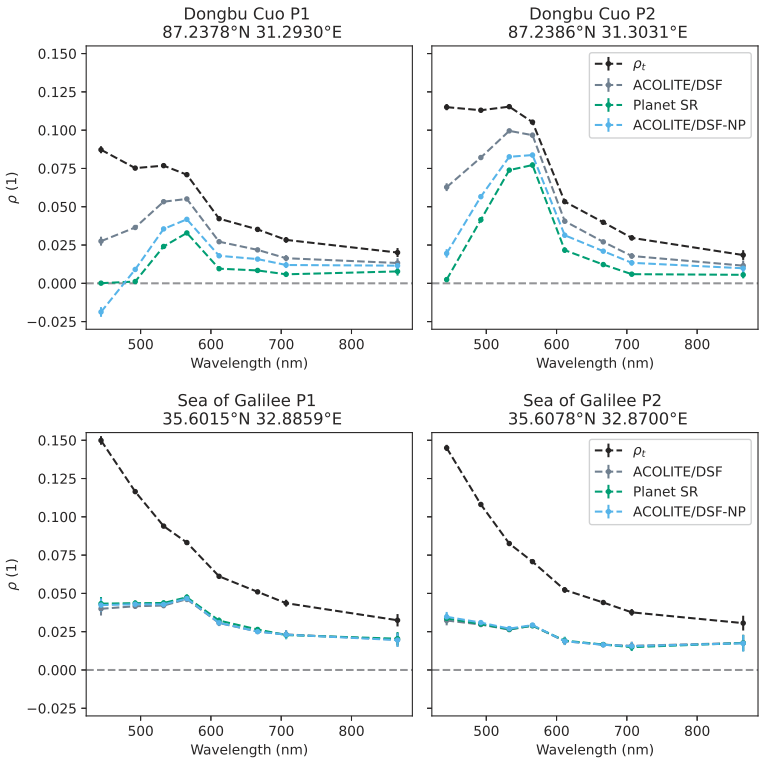

Fig. 12. Results for Dongbu Cui on 2022-11-13 at 04:30 UTC (Dove 2484, top) and for the Sea of Galilee on 2022-11-18 at 07:20 UTC (Dove 2449, bottom). ACOLITE results are shown with (DSF) and without (DSF-NP) DEM derived pressure. Points represent the mean average over 11x11 pixels, with the error bars the standard deviation.

Optics EXPRESS

Appendix B: Clear water sun glint correction

In this appendix the use of NIR based glint correction methods is demonstrated for waters with a negligible NIR signal originating from below the air-water interface. SuperDoves have no glint mitigation, and especially for lower latitudes, the presence of glint reflectance (ρ_g) in the observations can be problematic. Imagery under various glint conditions was obtained for the Hogsty Reef, a remote coral atoll in the Bahamas (at around 21.6833°N, 73.8167°W). Hogsty Reef (Fig. 13) is characterised by a bright visible sea bottom, with depths mostly less than 15 m, and lagoon depths between 6–8 m [45,46], with low turbidity water and hence zero NIR water reflectance. The reef is largely below the water surface, except for two small sandy islands, labeled N and S in Fig. 13. Due to the location of the atoll, satellite imagery is frequently affected by significant sun glint on the air-water interface. Per-pixel ρ_g is estimated by assuming ρ_s NIR can be fully attributed to the air-water interface, i.e. $\rho_s = \rho_g$ in the NIR band. ρ_g is then transferred from the NIR to the visible bands either by (1) the ratio of band average direct atmospheric transmittance and Fresnel reflectance ratios [42], (2) by results obtained using the OSOAA [47] radiative transfer model [14,48], or (3) by an image derived ratio [49–51]. All three options can be applied to DSF outputs, with options (1) and (2) fully automated, and directly integrated into ACOLITE as "default" and "alternative" glint correction methods respectively. Because option (3) does not rely on external inputs it can be applied to both DSF and PSR outputs. Reference pixels for option (3) to determine band specific glint scaling factors were selected using manual rectangular subsets on the image, located in the north east and north west corners of the image. The normalised difference water index (NDWI), [green-NIR]/[green+NIR] was evaluated to automatically determine pixels to estimate these factors, but was found to perform poorly in severely glinted conditions. Option (3) is here applied on ρ_s data, and hence with a zero offset in the NIR. SuperDove imagery was acquired with light glint on 2022-03-31 and 2022-09-09 (NIR $\rho_g < 0.008$), and with severe glint on 2022-06-29 (NIR $\rho_g > 0.06$).

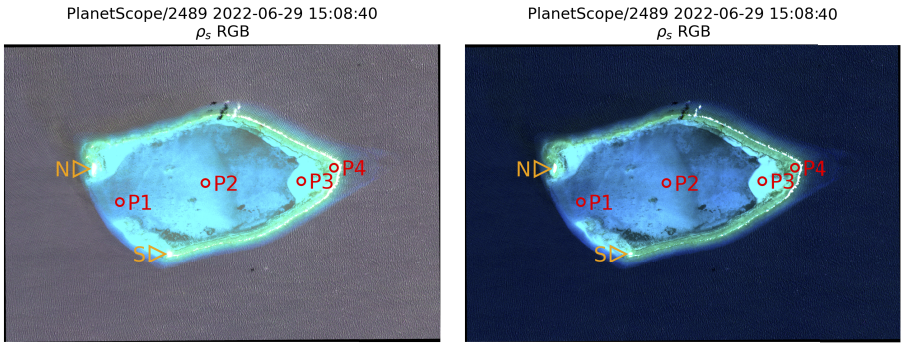

Fig. 13. ρ_s RGB composites for Hogsty Reef for the severely glinted image taken on 2022-06-29 (Dove 2489) from DSF outputs without (left), and with (right) the default glint correction. The results for the labeled points P1–4 are shown in Fig. 14. The entire reef is under water, apart from two small islands labeled N and S. Note the wave facets that are still present in the right image, i.e. after glint correction.

Output spectra before and after glint correction are evaluated using Hydrolight v5.3 [52] simulations in the 400–900 nm range (at 5 nm) using the "NewCase1" model for a range of water depths (D, from 0.1 to 50 m), chlorophyll a concentration (C, from 0.01 to 30 $mg \cdot m^{-3}$), and the various bottom types included in the Hydrolight distribution (B01–13). Hydrolight outputs are stored in a LUT and are convoluted to the SuperDove RSR. Reflectance spectra are extracted for four points across different water depths in the lagoon for imagery before and after glint correction (P1–4 in Fig. 13). Spectra are fitted to the Hydrolight LUT by optimisation of two free parameters

Optics EXPRESS

(*C* and *D*) for each bottom type (Fig. 14). LUT interpolation is performed in logarithmic space. Sandy bottom types "avg_ooid_sand" (7) and "coral_sand" (11) are most commonly retrieved, with in some cases "avg_dark_sediment" (3) "avg_hardpan" (4) being retrieved for the more shallow points. Between the lightly glinted scenes, retrieved bottom depths were quite well aligned without glint correction, within 1 m for the deepest points (P1 and P2), and within 0.1–0.4 m for the more shallow points (P3 and P4). The depths were likely underestimated due to the additional glint signal. For the severely glinted image, due to the shifted spectra the retrievals were meaningless, giving < 3 m depth for all four points, with differences to the lightly glinted scenes of 1.2–8.0 m. Especially the elevated reflectance in the Red, Red Edge, and NIR bands could not be fit to the water model. Using the default glint correction in ACOLITE, i.e. option (1) using Fresnel and direct transmittance ratios, the lightly glinted scenes agreement improved to within 0.2–1.1 m for the deepest point, and within 0.0–0.4 m for the more shallow points. For the severely glinted scene, the differences to the non-glinted scenes greatly reduced to 0.6–3.0 m, and a much better agreement to the model was found at longer wavelengths. The best fitting results were obtained for method (1), although other methods did not perform significantly worse, except for the severely glinted image, where more variable results were retrieved. Method (3) using image derived ratios performed worst for this image, giving an overestimation of depth, and overcorrection was clear, with negative reflectances being retrieved in the Yellow, Red, and Red Edge bands. In light glint conditions and for waters with negligible NIR signal the use of a glint correction can be recommended, and is fully automated in ACOLITE. In many cases, due to dense temporal coverage by SuperDove, severely glinted imagery can be excluded from analyses, although it is demonstrated here that reasonable corrections can be achieved.

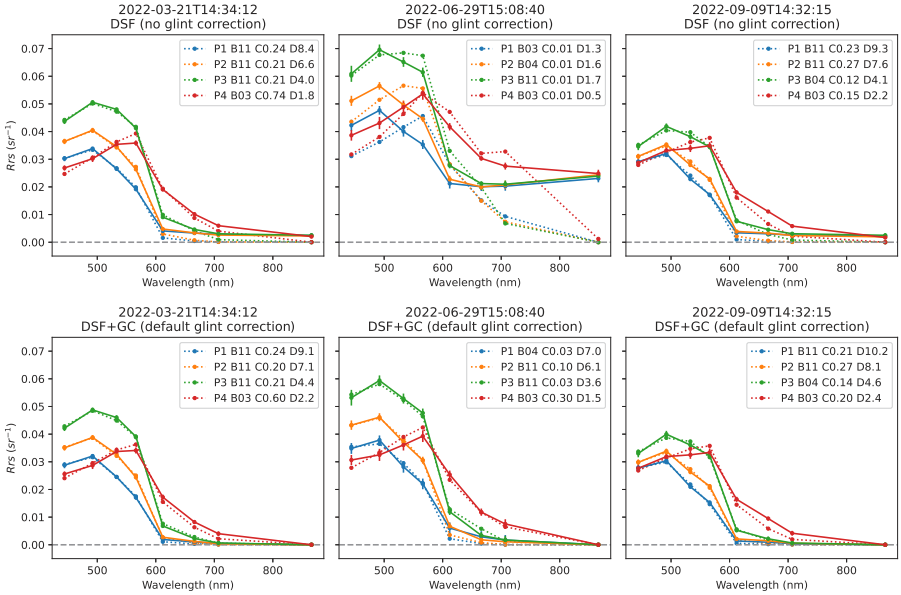

Fig. 14. Remote sensing reflectance (*Rrs*, in sr^{-1}) for Hogsty Reef for two dates with light glint (left and right, Dove 241b, 2022-03-31 and Dove 2429, 2022-09-09) and severe glint (middle, Dove 2489, 2022-06-29). Results are for DSF without (top) and with (bottom) the default glint correction using Fresnel and direct transmittance ratios. Solid lines show the mean average spectra extracted for 11x11 pixel boxes, with the error bars the standard deviation. The dotted line shows the Hydrolight results fitted to the mean spectra, with the labels indicating the retrieved bottom type (*B*, 01–13), chlorophyll *a* concentration (*C*, in $mg \cdot m^3$), and depth (*D*, in *m*).

Optics EXPRESS

Funding. European Space Agency (HYPERNET-VN).

Acknowledgments. Planet is thanked for research access to SuperDove data. The Flemish Marine Institute (VLIZ) and POM West-Vlaanderen are thanked for access to the Blue Accelerator Platform in Oostende, Belgium, and installation support. Dieter Vansteenwegen is thanked for technical support and installation of the PANTHYR. Meetnet Vlaamse Banken is thanked for providing wind, pressure, and tide gauge data from their Oostende Weather Station and Harbour sites. Kevin Ruddick and Alexandre Castagna are thanked for feedback and discussions about SuperDove applications. Two anonymous reviewers are thanked for their comments.

Disclosures. The author declares that there are no conflicts of interest related to this article.

Data availability. Data underlying the results presented in this paper are not publicly available but may be obtained from the author after agreement with the original data provider.

References

1. Q. Vanhellemont and K. Ruddick, "Turbid wakes associated with offshore wind turbines observed with Landsat 8," Remote. Sens. Environ. **145**, 105–115 (2014).
2. A. Ody, D. Doxaran, Q. Vanhellemont, B. Nechad, S. Novoa, G. Many, F. Bourrin, R. Verney, I. Pairaud, and B. Gentili, "Potential of High Spatial and Temporal Ocean Color Satellite Data to Study the Dynamics of Suspended Particles in a Micro-Tidal River Plume," Remote. Sens. **8**(3), 245 (2016).
3. S. Novoa, D. Doxaran, A. Ody, Q. Vanhellemont, V. Lafon, B. Lubac, and P. Gernez, "Atmospheric corrections and multi-conditional algorithm for multi-sensor Remote. Sens. of suspended particulate matter in low-to-high turbidity levels coastal waters," Remote. Sens. **9**(1), 61 (2017).
4. B. A. Franz, S. W. Bailey, N. Kuring, and P. J. Werdell, "Ocean color measurements with the Operational Land Imager on Landsat-8: implementation and evaluation in SeaDAS," J. Appl. Remote. Sens. **9**(1), 096070 (2015).
5. C. Kuhn, A. de Matos Valerio, N. Ward, L. Loken, H. O. Sawakuchi, M. Kampel, J. Richey, P. Stadler, J. Crawford, R. Striegl, E. Vermote, N. Pahlevan, and D. Butman, "Performance of Landsat-8 and Sentinel-2 surface reflectance products for river Remote. Sens. retrievals of chlorophyll-a and turbidity," Remote. Sens. Environ. **224**, 104–118 (2019).
6. A. Pacheco, J. Horta, C. Loureiro, and Ó. Ferreira, "Retrieval of nearshore bathymetry from Landsat 8 images: A tool for coastal monitoring in shallow waters," Remote. Sens. Environ. **159**, 102–116 (2015).
7. I. Caballero and R. P. Stumpf, "Retrieval of nearshore bathymetry from Sentinel-2A and 2B satellites in South Florida coastal waters," Estuarine, Coastal Shelf Sci. **226**, 106277 (2019).
8. A. Dogliotti, J. Gossn, Q. Vanhellemont, and K. Ruddick, "Detecting and Quantifying a Massive Invasion of Floating Aquatic Plants in the Río de la Plata Turbid Waters Using High Spatial Resolution Ocean Color Imagery," Remote. Sens. **10**(7), 1140 (2018).
9. N. Pahlevan, A. Mangin, and S. V. Balasubramanian, *et al.*, "ACIX-Aqua: A global assessment of atmospheric correction methods for Landsat-8 and Sentinel-2 over lakes, rivers, and coastal waters," Remote. Sens. Environ. **258**, 112366 (2021).
10. Q. Vanhellemont and K. Ruddick, "Atmospheric correction of metre-scale optical satellite data for inland and coastal water applications," Remote. Sens. Environ. **216**, 586–597 (2018).
11. Y. Luo, D. Doxaran, and Q. Vanhellemont, "Retrieval and Validation of Water Turbidity at Metre-Scale Using Pléiades Satellite Data: A Case Study in the Gironde Estuary," Remote. Sens. **12**(6), 946 (2020).
12. J. Pitarch and Q. Vanhellemont, "The QAA-RGB: A universal three-band absorption and backscattering retrieval algorithm for high resolution satellite sensors. Development and implementation in ACOLITE," Remote. Sens. Environ. **265**, 112667 (2021).
13. Q. Vanhellemont, "Daily metre-scale mapping of water turbidity using CubeSat imagery," Opt. Express **27**(20), A1372–A1399 (2019).
14. Q. Vanhellemont, "Sensitivity analysis of the dark spectrum fitting atmospheric correction for metre-and decametre-scale satellite imagery using autonomous hyperspectral radiometry," Opt. Express **28**(20), 29948–29965 (2020).
15. A. S. Mansaray, A. R. Dzialowski, M. E. Martin, K. L. Wagner, H. Gholizadeh, and S. H. Stoodley, "Comparing PlanetScope to Landsat-8 and Sentinel-2 for sensing water quality in reservoirs in agricultural watersheds," Remote. Sens. **13**(9), 1847 (2021).
16. M. Niroumand-Jadidi, C. J. Legleiter, and F. Bovolo, "Bathymetry retrieval from CubeSat image sequences with short time lags," Int. J. Appl. Earth Obs. Geoinformation **112**, 102958 (2022).
17. M. Niroumand-Jadidi, C. J. Legleiter, and F. Bovolo, "River Bathymetry Retrieval From Landsat-9 Images Based on Neural Networks and Comparison to SuperDove and Sentinel-2," IEEE J. Sel. Top. Appl. Earth Observations Remote Sensing **15**, 5250–5260 (2022).
18. A. Collison, A. Jumpasut, and H. Bourne, *On-orbit Radiometric Calibration of the Planet Satellite Fleet* (Planet Labs PBC, https://assets.planet.com/docs/radiometric_calibration_white_paper.pdf, accessed 2022-11-21, 2022).
19. S. G. Simis, S. W. Peters, and H. J. Gons, "Remote. Sens. of the cyanobacterial pigment phycocyanin in turbid inland water," Limnology and oceanography **50**(1), 237–245 (2005).
20. A. Castagna, S. Simis, H. Dierssen, Q. Vanhellemont, K. Sabbe, and W. Vyverman, "Extending Landsat 8: Retrieval of an orange contra-band for inland water quality applications," Remote. Sens. **12**(4), 637 (2020).

Optics EXPRESS

21. H. J. Gons, "Optical teledetection of chlorophyll a in turbid inland waters," Environ. Sci. Technol. **33**(7), 1127–1132 (1999).
22. K. G. Ruddick, H. J. Gons, M. Rijkeboer, and G. Tilstone, "Optical Remote. Sens. of chlorophyll a in case 2 waters by use of an adaptive two-band algorithm with optimal error properties," Appl. Opt. **40**(21), 3575–3585 (2001).
23. Q. Vanhellemont, "Adaptation of the dark spectrum fitting atmospheric correction for aquatic applications of the Landsat and Sentinel-2 archives," Remote. Sens. Environ. **225**, 175–192 (2019).
24. H. Lavigne, K. Ruddick, and Q. Vanhellemont, "Monitoring of high biomass Phaeocystis globosa blooms in the Southern North Sea by in situ and future spaceborne hyperspectral radiometry," Remote. Sens. Environ. **282**, 113270 (2022).
25. D. Vansteenwegen, K. Ruddick, A. Cattrijsse, Q. Vanhellemont, and M. Beck, "The pan-and-tilt hyperspectral radiometer system (PANTHYR) for autonomous satellite validation measurements-Prototype design and testing," Remote. Sens. **11**(11), 1360 (2019).
26. C. D. Mobley, "Estimation of the remote-sensing reflectance from above-surface measurements," Appl. Opt. **38**(36), 7442–7455 (1999).
27. K. G. Ruddick, V. De Cauwer, Y.-J. Park, and G. Moore, "Seaborne measurements of near infrared water-leaving reflectance: The similarity spectrum for turbid waters," Limnol. Ocean. **51**(2), 1167–1179 (2006).
28. Q. Vanhellemont and K. Ruddick, "Atmospheric correction of Sentinel-3/OLCI data for mapping of suspended particulate matter and chlorophyll-a concentration in Belgian turbid coastal waters," Remote. Sens. Environ. **256**, 112284 (2021).
29. E. Vermote, D. Tanré, J. Deuzé, M. Herman, J. Morcrette, and S. Kotchenova, *Second simulation of a satellite signal in the solar spectrum-vector (6SV)* (NASA/GSFC, 2006).
30. E. Vermote, N. El Saleous, C. Justice, Y. Kaufman, J. Privette, L. Remer, J. Roger, and D. Tanre, "Atmospheric correction of visible to middle-infrared EOS-MODIS data over land surfaces: Background, operational algorithm and validation," J. Geophys. Res. **102**(D14), 17131–17141 (1997).
31. MODIS/Terra Aerosol Optical Thickness Daily L3 Global 0.05Deg CMAMODIS (2023). Accessed 26 March 2023.
32. A. Gitelson, "The peak near 700 nm on radiance spectra of algae and water: relationships of its magnitude and position with chlorophyll concentration," Int. J. Remote. Sens. **13**(17), 3367–3373 (1992).
33. R. Röttgers, R. Doerffer, D. McKee, and W. Schönfeld, "The Water Optical Properties Processor (WOPP): Pure Water Spectral Absorption, Scattering, and Real Part of Refractive Index Model," (2016).
34. F. H. Freitas and H. M. Dierssen, "Evaluating the seasonal and decadal performance of red band difference algorithms for chlorophyll in an optically complex estuary with winter and summer blooms," Remote. Sens. Environ. **231**, 111228 (2019).
35. A. A. Gitelson, G. Dall'Olmo, W. Moses, D. C. Rundquist, T. Barrow, T. R. Fisher, D. Gurlin, and J. Holz, "A simple semi-analytical model for remote estimation of chlorophyll-a in turbid waters: Validation," Remote. Sens. Environ. **112**(9), 3582–3593 (2008).
36. A. A. Gilerson, A. A. Gitelson, J. Zhou, D. Gurlin, W. Moses, I. Ioannou, and S. A. Ahmed, "Algorithms for remote estimation of chlorophyll-a in coastal and inland waters using red and near infrared bands," Opt. Express **18**(23), 24109–24125 (2010).
37. S. Mishra and D. R. Mishra, "Normalized difference chlorophyll index: A novel model for remote estimation of chlorophyll-a concentration in turbid productive waters," Remote. Sens. Environ. **117**, 394–406 (2012).
38. S. Sterckx, E. Knaeps, and K. Ruddick, "Detection and correction of adjacency effects in hyperspectral airborne data of coastal and inland waters: the use of the near infrared similarity spectrum," Int. J. Remote Sensing **32**(21), 6479–6505 (2011).
39. L. De Keukelaere, S. Sterckx, S. Adriaensen, E. Knaeps, I. Reusen, C. Giardino, M. Bresciani, P. Hunter, C. Neil, D. Van der Zande, and D. Vaiciute, "Atmospheric correction of Landsat-8/OLI and Sentinel-2/MSI data using iCOR algorithm: validation for coastal and inland waters," European Journal of Remote. Sens. **51**(1), 525–542 (2018).
40. F. Steinmetz, P.-Y. Deschamps, and D. Ramon, "Atmospheric correction in presence of sun glint: application to MERIS," Opt. Express **19**(10), 9783–9800 (2011).
41. S. Kay, J. D. Hedley, and S. Lavender, "Sun glint correction of high and low spatial resolution images of aquatic scenes: A review of methods for visible and near-infrared wavelengths," Remote. Sens. **1**(4), 697–730 (2009).
42. T. Harmel, M. Chami, T. Tormos, N. Reynaud, and P.-A. Danis, "Sunglint correction of the Multi-Spectral Instrument (MSI)-SENTINEL-2 imagery over inland and sea waters from SWIR bands," Remote. Sens. Environ. **204**, 308–321 (2018).
43. A. Castagna, L. Amadei Martínez, M. Bogorad, I. Daveloose, R. Dasseville, H. M. Dierssen, M. Beck, J. Mortelmans, H. Lavigne, A. Dogliotti, D. Doxaran, K. Ruddick, W. Vyverman, and K. Sabbe, "Optical and biogeochemical properties of diverse Belgian inland and coastal waters," Earth Syst. Sci. Data **14**(6), 2697–2719 (2022).
44. Copernicus DEM Global and European Digital Elevation ModelCopernicus (2023). Accessed 26 March 2023.
45. J. D. Milliman, "The geomorphology and history of Hogsty Reef, a Bahamian atoll," Bull. Mar. Sci. **17**, 519–543 (1967).
46. A. W. Bruckner, *Khaled bin Sultan Living Oceans Foundation Habitat Mapping and Coral Reef Assessments: Hogsty Reef, Great Inagua, and Little Inagua, Bahamas* (Khaled bin Sultan Living Oceans Foundation Publication #7, 2011).
47. M. Chami, B. Lafrance, B. Fougnie, J. Chowdhary, T. Harmel, and F. Waquet, "OSOAA: a vector radiative transfer model of coupled atmosphere-ocean system for a rough sea surface application to the estimates of the directional

Optics EXPRESS

variations of the water leaving reflectance to better process multi-angular satellite sensors data over the ocean," Opt. Express **23**(21), 27829–27852 (2015).
48. F. Braga, A. Fabbretto, Q. Vanhellemont, M. Bresciani, C. Giardino, G. M. Scarpa, G. Manfè, J. A. Concha, and V. E. Brando, "Assessment of PRISMA water reflectance using autonomous hyperspectral radiometry," ISPRS J. Photogramm. Remote. Sens. **192**, 99–114 (2022).
49. D. R. Lyzenga, "Shallow-water bathymetry using combined lidar and passive multispectral scanner data," Int. Journal Remote Sensing **6**(1), 115–125 (1985).
50. E. J. Hochberg, S. Andréfouët, and M. R. Tyler, "Sea surface correction of high spatial resolution ikonos images to improve bottom mapping in near-shore environments," IEEE Trans. Geosci. Remote Sensing **41**(7), 1724–1729 (2003).
51. J. Hedley, A. Harborne, and P. Mumby, "Simple and robust removal of sun glint for mapping shallow-water benthos," Int. J. Remote. Sens. **26**(10), 2107–2112 (2005).
52. J. D. Hedley, C. D. Mobley, and L. K. Sundman, *HYDROLIGHT 5.3 ECOLIGHT 5.3 Technical Documentation* (Sequoia Scientific Inc, 2017).